

The original publication is available at www.springerlink.com

Flow rate limitation of steady convective dominated open capillary channel flows through a groove

Dennis Haake · Joerg Klatte · Aleksander Grah · Michael E. Dreyer

Received: date / Accepted: date

Abstract An open capillary channel is a structure that establishes a liquid flow path when the capillary pressure caused by surface tension forces dominates in comparison to the hydrostatic pressure induced by gravitational or residual accelerations. To maintain a steady flow through the channel the capillary pressure of the free surface has to balance the pressure difference between the liquid and the surrounding constant pressure gas phase. Due to convective and viscous momentum transport the pressure along the flow path of the liquid decreases and causes the free surface to bend inwards. The maximum flow rate through the channel is reached when the free surface collapses and gas ingestion occurs near the outlet. This stability limit depends on the geometry of the channel and the properties of the liquid. In this paper we present an experimental setup which is used in the low-gravity environment of the Bremen Drop Tower. Experiments with convective dominated systems have been performed where the flow rate was increased up to the maximum value. In comparison to this we present a one-dimensional theoretical model to determine important characteristics of the flow, such as the free surface shape and the limiting flow rate. Furthermore we present an explanation for the mechanism of flow rate limitation for these flow conditions which is similar to the choking problem for compressible gas flows.

Keywords Free Surface Flow · Capillary Channel · Critical · Convective Dominated · Microgravity

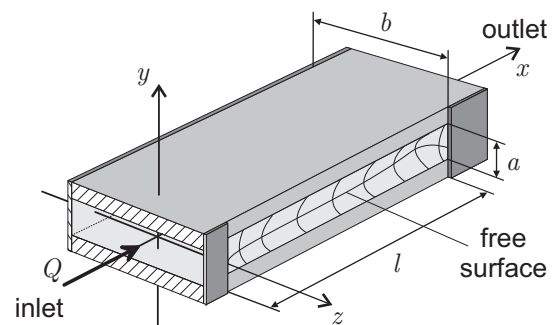


Fig. 1 Schematic drawing of the flow with a constant flow rate Q through a groove of width a , depth b and length l .

1 Introduction

Open capillary channels are used in a number of applications related to space liquid management, i.e. heat pipes in the thermal systems and propellant management devices (PMD) in surface tension tanks of satellites. Concerning the latter, open channels are often used for transport and positioning of liquid propellants (see e.g. in [1] or [2]).

Rosendahl *et al.* (2004) [3] found a flow limitation in open capillary channels which is similar to choking in compressible duct flows and open channel flows under gravity. In this work we want to expand this theory to other channel geometries.

In our investigation the capillary channel consists of two parallel glass plates with a free surface at one side and a closed plate at the other side (see Fig. 1), hereinafter referred to as groove. The liquid flows along the x -axis from the inlet to the outlet and forms a free surface at the open side between the plates. The flow is maintained by an external pump while the free surface deforms corresponding to the pressure along the flow path.

D. Haake · J. Klatte · A. Grah · M. E. Dreyer
Center of Applied Space Technology and Microgravity
Am Fallturm, 28359 Bremen, Germany
Tel.: +49-421-218-4038
Fax: +49-421-218-2521
E-mail: dreyer@zarm.uni-bremen.de

For an internal pressure p lower than the ambient pressure p_a , the free liquid surface is concave at any cross section, as shown in Fig. 1. The pressure decreases in flow direction due to convective and viscous momentum transport so that the curvature of the surface increases and the flow path constricts. A steady flow is obtained only for a flow rate Q below a critical value Q_{crit} . For $Q > Q_{crit}$ the liquid surface collapses at the channel outlet and the flow changes from steady single-phase flow to unsteady two-phase flow.

To minimize the influence of the hydrostatic pressure on the capillary channel the experiments have been performed in the microgravity environment of the Bremen Drop Tower.

2 Theoretical model

For the theoretical model the flow is considered as incompressible and laminar with a Newtonian, perfectly wetting liquid. The gap distance, the width of the parallel plates and the length of the open channel are denoted by a , b and l , respectively. The model is restricted to steady single-phase flow conditions with subcritical flow rates ($Q < Q_{crit}$). The flow along the channel axis x is assumed to be one-dimensional and is characterized by the mean velocity v and the liquid pressure p .

2.1 Scaling and characteristic numbers

Here and in the following all variables are considered non-dimensional. In our model all lengths are scaled with a quarter of the hydraulic diameter of the open channel, except the x -direction, which is scaled with the channel length l . The hydraulic diameter d_h of the groove is defined as [4]

$$d_h = \frac{4ab}{2b + a}. \quad (1)$$

The curvature of the free surface h is scaled by $4/d_h$ and the pressure p by $4\sigma/d_h$, where σ is the surface tension of the fluid. The cross section area of the groove A , which is shown in Fig. 2, is scaled by the inlet cross section area $A_0 = ab$ and velocities are scaled with the characteristic velocity (see Dreyer (2007) [5])

$$v_c = \sqrt{\frac{4\sigma}{\rho d_h}}, \quad (2)$$

whereas ρ denotes the fluid density. The flow rate Q is scaled with $A_0 v_c$.

The describing characteristic numbers are the Ohnesorge number

$$\text{Oh} = \sqrt{\frac{\rho \nu^2}{\sigma d_h}}, \quad (3)$$

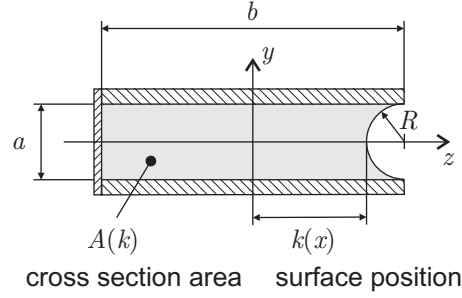


Fig. 2 Cross section of the capillary channel in the (y, z) -plane at constant x .

the dimensionless channel length

$$\tilde{l} = \frac{\text{Oh} l}{2d_h}, \quad (4)$$

and the aspect ratio

$$\Lambda = \frac{b}{a}. \quad (5)$$

The Ohnesorge number can be expressed as a Reynolds number, based on the characteristic velocity v_c , thus

$$\text{Oh} = \frac{2}{\text{Re}_c} \quad \text{with} \quad \text{Re}_c = \frac{d_h v_c}{\nu}, \quad (6)$$

whereas ν denotes the kinematic viscosity.

2.2 Governing equations

The first equation is the dimensionless Bernoulli equation [6] including a friction term w_f , differentiated in flow direction x

$$\frac{dp}{dx} + v \frac{dv}{dx} + \frac{dw_f}{dx} = 0. \quad (7)$$

The first term is the pressure gradient in x -direction, the second term specifies the convective acceleration due to area changes, and the third term is the irreversible pressure loss due to viscous forces which is for a fully developed flow

$$\frac{dw_f}{dx} = \frac{K_{pf}}{2} \tilde{l} v. \quad (8)$$

Therein, K_{pf} is the laminar friction factor for rectangular ducts, which is a function of the channel gap ratio Λ [6].

The second equation is the dimensionless conservation of mass for an incompressible fluid

$$\frac{dQ}{dx} = A \frac{dv}{dx} + v \frac{dA}{dx} = 0. \quad (9)$$

To calculate the cross-sectional area A in the (y, z) -plane a constant radius R is assumed at each cross-section (Fig. 2). Therefore the cross-section area is a function of the minimal contour value k , one of the main variables of the following differential equation system.

The detailed derivation of the governing equation for $A(k)$ can be found in Haake *et al.* (2006) [7].

The convective term of the Bernoulli equation [Eq. (7)] can be rewritten as

$$v \frac{dv}{dx} = -\frac{Q^2}{A^3} \frac{dA}{dx}, \quad (10)$$

applying the conservation of mass [Eq. (9)].

Assuming zero normal and tangential stresses at the free surface and a passive overlaying gas, the capillary pressure

$$p - p_a = -h = -\left(\frac{1}{R_1} + \frac{1}{R_2}\right) \quad (11)$$

is related to the curvature of the free surface by the Gauss-Laplace equation [8], where $h/2$ is the mean curvature of the liquid surface. Here, R_1 and R_2 are the principal radii of the free surface curvature. R_1 is the radius of curvature in a plane perpendicular to the (x, z) -plane containing the normal of the free surface at $y = 0$. R_2 is the radius of curvature in the (x, z) -plane [3]. Since the ambient pressure p_a is constant, the pressure gradient reads

$$\frac{dp}{dx} = -\frac{dh}{dx}. \quad (12)$$

To solve the differential equation, the mean curvature h must be defined as a function of the surface position k and its derivatives in x -direction. The assumption of symmetry with respect to the (x, z) -plane reduces the general form of the mean surface [9] to

$$h(x, y = 0) = \frac{1}{R_1} + \frac{\Gamma^2 d^2 k / dx^2}{\left[1 + \Gamma^2 (dk/dx)^2\right]^{3/2}} \quad (13)$$

with the coefficient

$$\Gamma = \frac{d_h}{4l}. \quad (14)$$

Again, if a constant radius at the mean curvature plane for R_1 is assumed, the principal radius of surface curvature R_1 is a function of k only [7]. This assumption disagrees with the earlier assumption of a constant radius in the (y, z) -plane, but reduces the complexities of this problem from 3-D to 1-D. Anyway, in this context the accuracy has been proved by 3-D solutions of the mean surface curvature equations (Klatte *et al.* [10]).

Substituting the capillary pressure (Eq. (12)), the convective term (Eq. (10)) and the pressure loss (Eq. (8)) into the Bernoulli equation (Eq. (7)), and applying Eq. (13) yields the final equations

$$\frac{dh}{dx} + \frac{Q^2}{A^3} \frac{dA}{dk} \frac{dk}{dx} - \frac{K_{pf}}{2} \frac{\tilde{l} Q}{A} = 0 \quad (15)$$

and

$$\Gamma^2 \frac{d^2 k}{dx^2} + \left(\frac{1}{R_1} - h\right) \left[1 + \Gamma^2 \left(\frac{dk}{dx}\right)^2\right]^{3/2} = 0. \quad (16)$$

Together with the equations for $A(k)$ and $R_1(k)$, this differential equation system can evaluate the contour function $k(x)$ and the mean curvature pressure $h(x)$.

2.3 Boundary conditions

The boundary conditions are given by the pinned surface at the edges of the channel inlet and outlet

$$k(x = 0) = k(x = 1) = \frac{2A + 1}{2} \quad (17)$$

and the surface curvature at the channel inlet

$$h(x = 0) = h_0. \quad (18)$$

The exact determination of the channel inlet curvature h_0 is described in Sec. 3.1.

2.4 Numerical procedure

For the numerical solution of the coupled nonlinear system (Eq. (15) and Eq. (16)) we treat h and k as variables and use second order central differences. The steady flow solution is solved with a damped Newton method and yields the liquid surface position $k(x) = f(\text{Oh}, A, \tilde{l}, Q)$ as well as the velocity $v(x)$, the cross-section $A(x)$, and the curvature $h(x)$ with the same dependence. As the numerical critical flow rate Q_{crit}^{num} , we define the maximum flow rate Q leading to the convergence of the numerical algorithm with a relative error of 10^{-8} [see also Grah *et al.* (2008)] [11].

3 Experimental setup

The experimental setup has been developed to operate with the new catapult system within a drop capsule at the Bremen Drop Tower which is presented in Fig. 3. With the catapult system the free fall time can be doubled and provides a microgravity time of about 9.35 s with a residual acceleration less than $10^{-5} g$.

Fig. 4 shows a schematic drawing of the experimental setup. The experimental setup consists of a fluid container filled with test liquid and the groove which is fixed upright on the reservoir. A pump enables a closed fluid circuit. The pump withdraws the liquid at the outlet of the groove and feeds it into the fluid container. Before entering the groove, the flow is accelerated and rectified by a nozzle. Differences in volume after gas ingestion are balanced by the compensation tube.

To guarantee gas-free liquid supply to the groove a screen is installed in the fluid container for the case that the setup is running at supercritical conditions with gas ingestion.

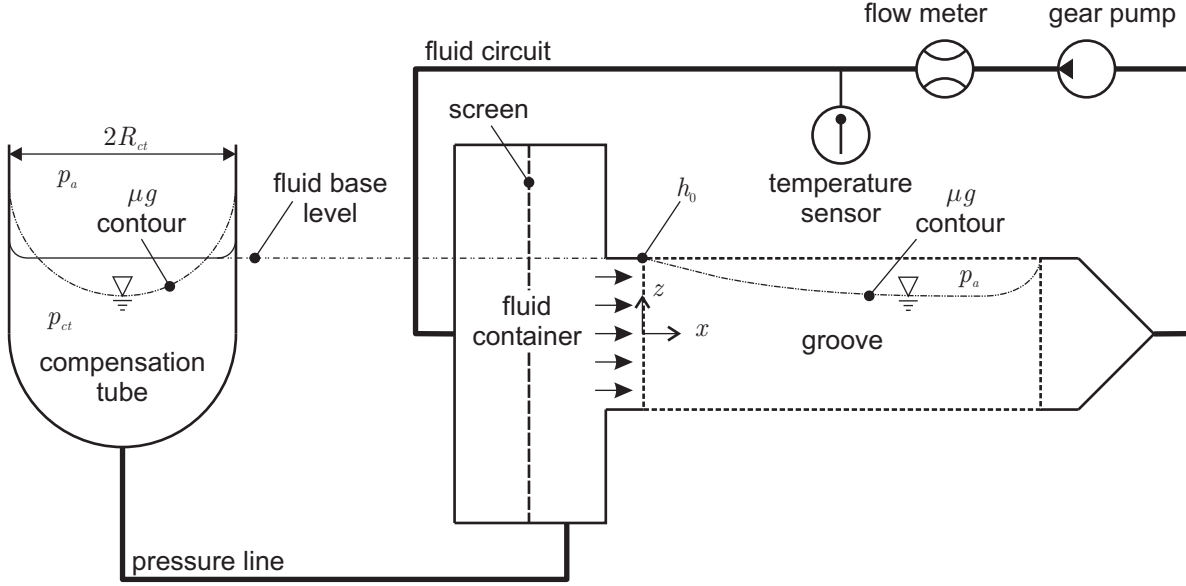


Fig. 4 Schematic drawing of the experimental setup with the test channel (dashed), the compensation tube, and the fluid circuit.

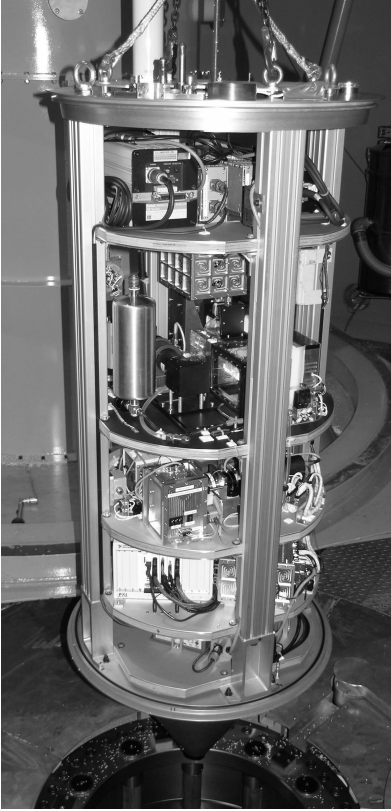


Fig. 3 Drop capsule with integrated experimental setup.

In the fluid container the pressure is predetermined by the curvature of the free surface in the compensation tube and the ambient pressure p_a . The boundary condition of the inlet curvature of the groove h_0 depends

on the pressure in the fluid container, the convective and the frictional flow losses in the nozzle.

3.1 Channel inlet boundary condition

Due to the complex geometry, no analytical data for the determination of the boundary condition h_0 are available in sufficient accuracy and a direct measurement was not possible. For this reason, we performed three-dimensional model computations using the volume of fluid code FLOW-3D (TM) (Version 8.1.1, Flow Science Inc.).

The curvature at the channel inlet h_0 is defined by the capillary pressure of the meniscus in the compensation tube p_{ct} including convective and frictional flow losses inside the liquid reservoir and the nozzle. The pressure loss is linear versus the Reynolds number [6] and the regression of the numerical data yields the relation

$$h_0 = \frac{K_1}{2} Q^2 + \frac{K_2 \text{Oh}}{4} Q + K_3 \quad (19)$$

with

$$K_3 = \frac{2}{R_{ct}}. \quad (20)$$

Therein R_{ct} is the dimensionless radius of the compensation tube. The values of $K_{1,2,3}$ are $K_1 = 1.49$, $K_2 = 383$ and $K_3 = 0.159$.

In order to obtain the best approximation to the one-dimensional model assumption, the flow path from the fluid container to inlet of the open capillary channel was optimized. The three-dimensional model computations led to a nozzle with a rectangular inlet cross

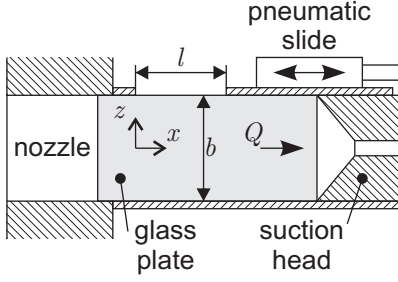


Fig. 5 Schematic drawing of the groove channel with the pneumatic slide.

section ($30 \times 50 \text{ mm}^2$) that converges to the channel cross section. The nozzle has an elliptical shape in the (x, y) -plane but no constriction in the (x, z) -plane and a length of 40 mm. With this shape, the lateral velocity components in the channel entrance cross section are minimized to less than 2% of the longitudinal component.

3.2 Experiment procedure

In Fig. 5 a detailed sketch of the capillary groove channel is presented. The three closed sides of the groove consist of three quartz glass plates which are glued together. Beyond the free surface area the open side is covered by a thin wettable tape of the company 3M (TM). This tape provides a well-defined open length l and sharp pinning edges for the free surface at the in- and outlet (Fig. 7b)). The pneumatic slide is mounted above the tape and is able to open and close the free surface area by a fast lateral motion.

In the initial configuration the channel is closed by the pneumatic slide and the flow is established through the closed channel with the desired constant volumetric flow rate Q . The channel is closed to minimize the perturbation on the fluid flow due to the initial acceleration of the drop capsule with the catapult system. At the beginning of the free fall period of the capsule the pneumatic slide moves away. Within the 9 s of free fall time the reorientation of the free surface and the fluid flow in microgravity conditions can be observed.

To determine the experimental critical flow rate Q_{crit}^{exp} , several experiments at different flow rates must be performed. The experimental critical flow rate Q_{crit}^{exp} is defined by

$$Q_{crit}^{exp} = \frac{1}{2} (Q_{max}^{st} + Q_{min}^{unst}), \quad (21)$$

where Q_{max}^{st} is the highest flow rate with steady flow and Q_{min}^{unst} the lowest flow rate leading to the collapse of the free surface.

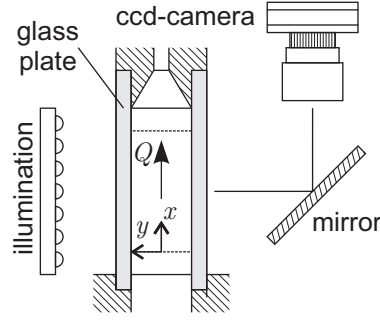


Fig. 6 Schematic drawing of the groove channel and optics.

Table 1 Experiment parameters with channel width a , channel depth b , aspect ratio A , dimensionless channel length \tilde{l} and Ohnesorge number Oh . The laminar friction factor for both channels reads $K_{pf} = 78.81$ [6].

| No. | a [mm] | b [mm] | l [mm] | A [-] | \tilde{l} [-] | Oh [-] |
|-----|----------|----------|----------|---------|-----------------------|-----------------------|
| 1 | 5 | 30 | 47.5 | 6.0 | 4.17×10^{-3} | 1.62×10^{-3} |
| 2 | 5 | 30 | 28.9 | 6.0 | 2.54×10^{-3} | 1.62×10^{-3} |

Table 2 Properties of test liquid FC-72 at 25°C [13]. The static contact angle is $\gamma_{stat} = 0$ on glass.

| Liquid | ρ [kg m^{-3}] | ν [$\text{m}^2 \text{s}^{-1}$] | σ [N m^{-1}] |
|--------|-------------------------------|--------------------------------------|--------------------------------|
| FC-72 | 1680.0 | 0.380×10^{-6} | 0.010 |

3.3 Flow observation and image processing

For flow observation a high speed CCD camera with 250 frames per second and a resolution of 512×480 pixel is used. The optical axis of the camera is aligned normal to the glass plates (see Fig. 6). For comparison with the numerical data, the surface profiles $k(x)$ were detected with a 5×5 Sobel technique [12] using the maximal gradient.

3.4 Parameters and experiments

Table 1 shows the parameters for the experiment campaigns. The properties of the test liquid FC-72 is provided in Table 2.

The low Ohnesorge numbers are typical for short length convection-dominated flows. For the shorter dimensionless channel length \tilde{l} , viscous effects are negligible. The longer channel is affected by viscous effects but remains convective dominated (see also Sec. 4.2).

To determine the critical flow rate Q_{crit} 12 drop experiments with different flow rates have been performed for each channel geometry.

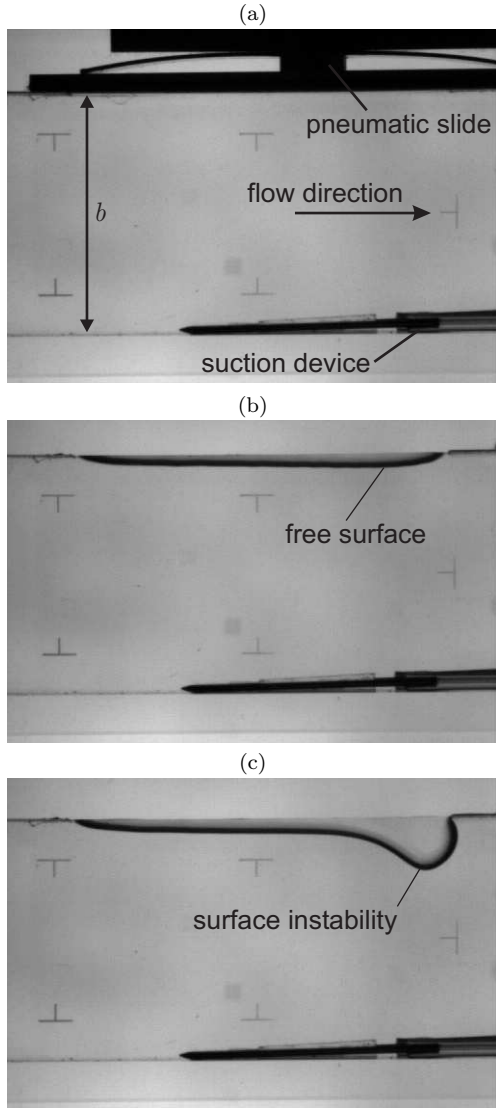


Fig. 7 (a) Detailed view of the groove at initial condition with closed pneumatic slide and developed flow. The flow direction is from left to right. (b) Experimental result of a subcritical flow rate in microgravity with a stable free surface. (c) In contrary a supercritical flow rate with an unstable free surface.

4 Results and discussion

In the following video images of the experimental observation with different flow conditions in the capillary channel are presented. Later the experimental data and the theoretical model are compared. Finally, the principle mechanism of flow rate limitation will be explained.

Fig. 7a shows a video image of the initial configuration. The suction device at the lower side is placed outside the channel to remove surplus liquid. The channel is closed by the pneumatic slide but the flow is already established. At the beginning of the microgravity condition the slide opens the channel and the free surface is established as shown in Fig. 7b. The experiment

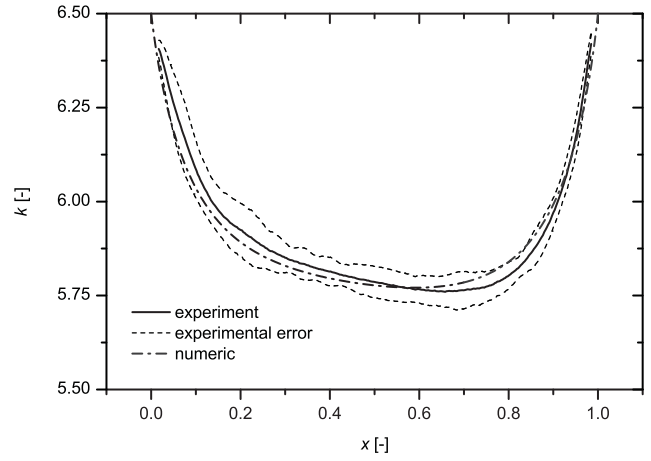


Fig. 8 Surface profile of the shorter channel at flow rate $Q = 0.827$ which is 90% of the numerical critical flow rate for this channel geometry.

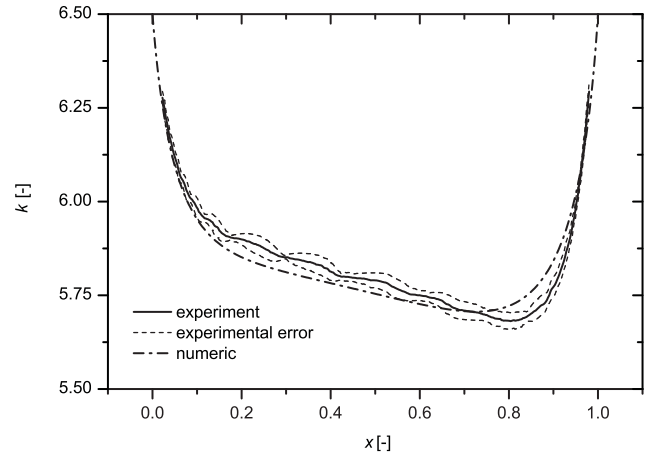


Fig. 9 Surface profile of the longer channel at flow rate $Q = 0.814$ which is 93% of the numerical critical flow rate for this channel geometry.

with a subcritical flow rate has a stable free surface and no gas ingestion at the channel outlet. In contrast Fig. 7c shows a supercritical system with an unstable free surface draining a gas bubble into the channel.

4.1 Comparison of experiment and theory

Fig. 8 shows the comparison for the short channel ($l = 28.9$ mm). For this case the wall shear stress is almost negligible (Sec. 4.2). The surface contour is plotted versus the flow direction x from the channel inlet $x = 0$ to the channel outlet $x = 1$. The contour plots correspond to a high flow rate ($Q = 0.827$) which is about 90% of the numerical critical flow rate for this channel geometry. Due to pressure perturbations from the gear pump small fluctuations can be observed at the free surface. To eliminate this dynamic effect the time averaged value over 250 video images (1 s) has been taken

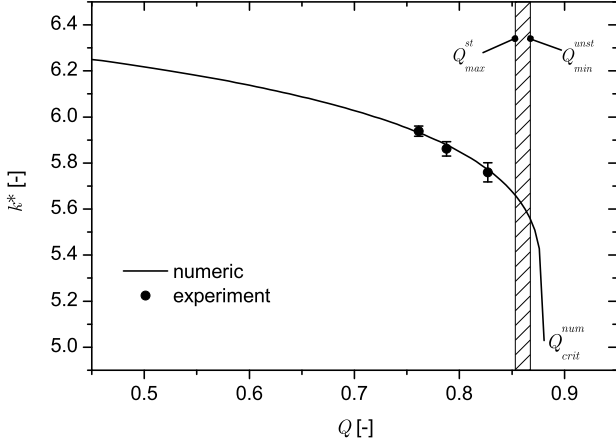


Fig. 10 Comparison of the experimental and numerical minimum contour position k^* for the shorter channel.

to get a steady surface contour. The experimental error shows the limits of the free surface within these 250 images. Fig. 8 shows a good agreement of the experimental and the numerical surface profile. The numerical surface contour is always bounded between the error lines of the experimental data. The maximum relative difference

$$\Delta k_{rel} = \max \left| \frac{k_{aver}^{exp}(x) - k^{num}(x)}{k^{num}(x)} \right| \quad (22)$$

between the average experimental contour $k_{aver}^{exp}(x)$ and the numerical solution $k^{num}(x)$ is smaller than 1%. For this short length l the convective term dominates and the contour is nearly symmetric to the middle of the channel.

For the longer channel ($l = 47.5$ mm), again at a high flow rate ($Q = 0.814$) which is about 93% of the numerical critical flow rate for this channel geometry, a good agreement of the experimental and numerical surface contour (Fig. 9) can be observed. According to the longer channel, the influence of friction increases (see Sec. 4.2). Therefore the innermost points are lower and the contours are not as symmetric as for the short channel. The deviation near the innermost point of the free surface is induced by the two radii-approximation. For high curvature deformation the assumption of the constant first principle radius R_1 is not exact. However, the accuracy is still good. The maximum relative difference Eq. (22) is smaller than 1.5%.

In Fig. 10 and 11 we compare the minimum contour point k^* versus the established flow rate Q . For increasing flow rates the surface bends inwards and collapses at the critical flow rate.

In Fig. 10, the results of the shorter channel are shown. The numerical and the experimental minimum contour points are in good agreement. Again, the error bars are influenced by the fluctuation of the free

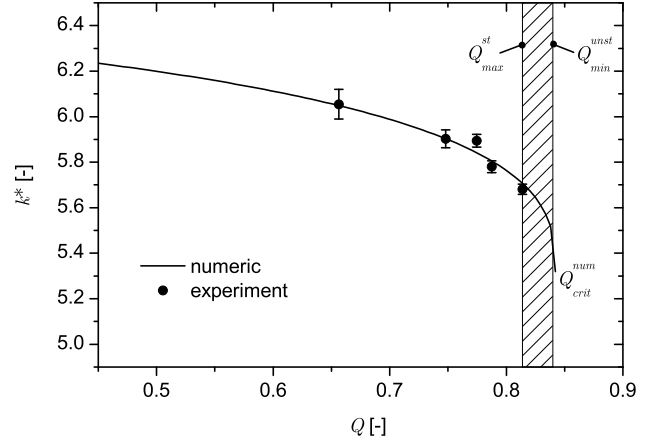


Fig. 11 Comparison of the experimental and numerical minimum contour position k^* for the longer channel.

surface. The experimental critical flow rate is shown as a single point. Here we get a critical flow rate area which is between the maximum stable $Q_{max}^{st} = 0.853$ and the minimum unstable case $Q_{min}^{unst} = 0.866$. This yields an experimental critical flow rate according to Eq. (21) as $Q_{crit}^{exp} = 0.86$. The numerical critical flow rate for this case is $Q_{crit}^{num} = 0.88$. The lower experimental critical flow rate is linked to the determination of this value. The experimental microgravity time is limited and the initial reorientation of the free surface cannot be avoided. Close to the critical flow rate a collapse of the free surface can occur during the dynamic reorientation. This is not captured by the numerical steady-state analysis. Anyway, the numerical value is in good agreement to the experimental flow rate. Also the results for the longer channel (Fig. 11) show good agreement for the minimum contour point versus the established flow rate and for the critical flow rate ($Q_{crit}^{exp} = 0.826$ and $Q_{crit}^{num} = 0.84$). The influence of friction increases for the long channel and the initial dynamic of the reorientation is damped faster. Therefore the numerical and experimental flow rates are in better agreement.

4.2 Classification of flow regime

To study the influence of the channel length l a parametric study of \tilde{l} for $Oh = 1.62 \times 10^{-3}$, $A = 6.0$ and fixed boundary conditions according to Eq. (19) has been done numerically. For each \tilde{l} the maximum flow rate Q_{crit}^{num} and the corresponding mean curvature difference between the channel inlet and outlet

$$\Delta h = h(x = 1) - h(x = 1) \quad (23)$$

were determined. The result is plotted in Fig. 12. Since the convective momentum transport in the channel is

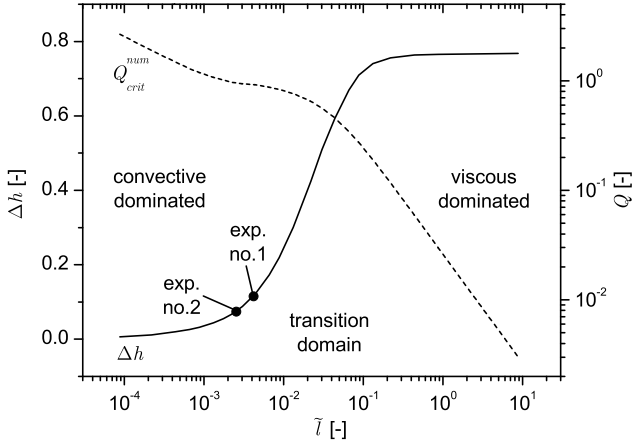


Fig. 12 Parametric study of the influence of the dimensionless channel length \tilde{l} on the irreversible pressure loss Δh (solid line) at the critical flow rate Q_{crit}^{num} (dashed line). The solutions for the channel geometry (Tab. 1) are denoted as exp.no.1 and exp.no.2. The Ohnesorge number is constant ($Oh = 1.62 \times 10^{-3}$) as well as the aspect ratio ($A = 6.0$).

reversible, it does not affect the pressure difference between the channel inlet and outlet, so Δh is a direct indicator for the influence of the irreversible, viscous pressure loss. For small channel lengths ($\tilde{l} < 10^{-3}$) the flow is dominated by convective momentum transport so the irreversible pressure loss Δh is small and the maximum flow rate is Q_{crit}^{num} is high. For long channels ($\tilde{l} > 10^{-1}$) the flow is dominated by viscous momentum transport. The reversible pressure loss due to convective momentum transport becomes negligible and the maximum flow rate Q_{crit}^{num} decreases to small values. Between these regimes the flow is controlled by both convective and viscous pressure losses.

As mentioned before both investigated channel types (see Tab. 1) are near the convective dominated domain. For this regime we present in the following the determining effect for the collapse of the free surface.

4.3 Mechanism of flow rate limitation

To describe the mechanism of flow rate limitation the numerical solutions of the capillary pressure and the local pressure at the smallest cross section (characterized with an asterisk) are compared. The capillary pressure is defined in Eq. (11)

$$h^* = \frac{1}{R_1} + \frac{1}{R_2} \quad (24)$$

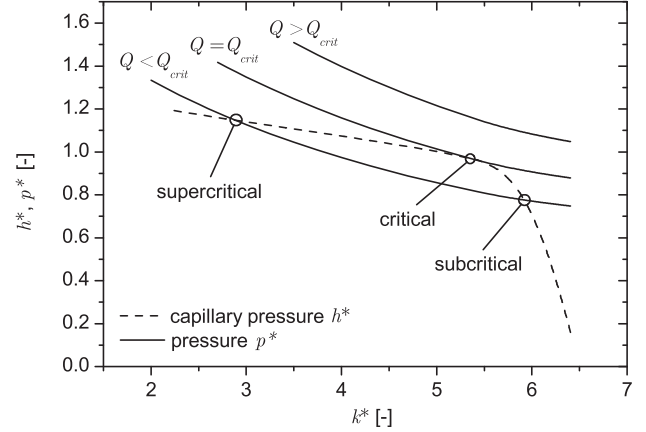


Fig. 13 Comparison of the numerical minimum solution for the capillary pressure h^* and local pressure $p^* = p_{conv}^* + \Delta p_{irr}$ of the shorter channel in dependence on k^* .

Substituting Eq. (12) and Eq. (8) in Eq. (7) and integration from the channel inlet to the smallest cross section yields

$$\underbrace{\frac{1}{R_1} + \frac{1}{R_2}}_{h^*} = \underbrace{\frac{1}{2} (v^{*2} - v_0^2)}_{p_{conv}^*} + \underbrace{h_0 + \frac{K_{pf}}{2} \tilde{l} \int_0^{x^*} v \, dx}_{\Delta p_{irr}}, \quad (25)$$

with the average velocity v_0 at the channel inlet. The capillary pressure h^* on the left hand side of Eq. (25) stabilizes the free surface. The convective pressure p_{conv}^* and the irreversible pressure loss Δp_{irr} with initial pressure h_0 on the right hand side destabilize the system.

In dependence on the minimum contour point k^* the capillary h^* and local pressure $p^* = p_{conv}^* + \Delta p_{irr}$ can be plotted for each channel geometry. In Fig. 13 the values for the shorter channel are applied. The local pressure p^* is dependent on the flow rate Q and is plotted for different established flow rates.

When the local pressure p^* and the capillary pressures h^* are equal a stationary solution is found. For flow rates lower than Q_{crit} subcritical and supercritical solutions exist. In the experiment only the subcritical solution can be reached because the supercritical solution is instable, but the numerical algorithm can calculate these points.

At the critical flow rate Q_{crit} we obtain only one solution. At this point the derivatives of the capillary and the convective pressure with respect to k^* are equal

$$\frac{dh^*}{dk^*} = \frac{dp^*}{dk^*}. \quad (26)$$

Due to the small frictional pressure loss for these channel types, the irreversible pressure loss Δp_{irr} is assumed

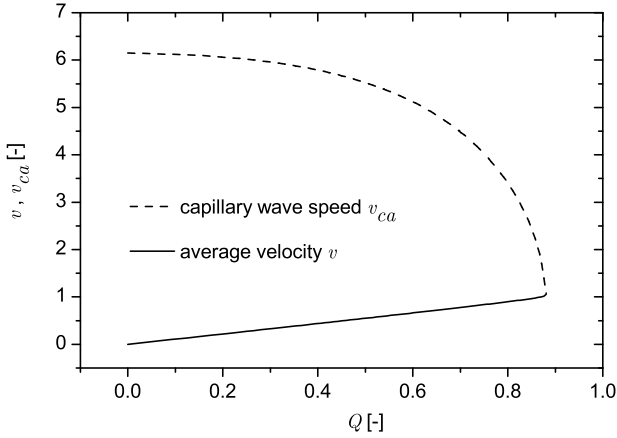


Fig. 14 Numerical solution of the capillary wave speed and the mean average flow velocity at the smallest cross section of channel no. 2 versus the flow rate.

as independent of k^* and the derivative with respect to k^* is equal to zero. With $v^* = Q/A^*$ it follows

$$\frac{dh^*}{dk^*} = \frac{d \left[\frac{1}{2} (Q_{crit}/A^*)^2 \right]}{dk^*}. \quad (27)$$

Only A^* and h^* are functions of k^* and the gradient of the convective pressure yields

$$\frac{dh^*}{dk^*} = -\frac{Q_{crit}^2}{A^{*3}} \frac{dA^*}{dk^*}. \quad (28)$$

Re-substitution of the mean velocity in the smallest cross section at the critical point v_{crit}^* reaches

$$\frac{Q_{crit}^2}{A^{*2}} = v_{crit}^{*2} = -A^* \frac{dh^*}{dA^*}. \quad (29)$$

The term on the right hand side of Eq. (29), formerly known as the small amplitude longitudinal wave speed v_{ca} defined by Rosendahl *et al.* [3], is

$$v_{crit}^{*2} = v_{ca}^2 = -A^* \frac{dh^*}{dA^*}. \quad (30)$$

This means that the limiting value of the flow through an open capillary groove is the average flow velocity at the smallest cross section. If the value reaches the small amplitude longitudinal wave speed the free surface collapses and the system becomes unstable. This phenomenon is similar to the choking problem for compressible gas flows, where the maximum mass flow is reached when the average flow velocity reaches the speed of sound [6].

Fig. 14 shows the numerical solution for the mean flow velocity and the calculated wave speed which is dependent on the flow rate. At the critical flow rate both velocities are equal and the flow is choked.

4.4 Comparison to other open channels

As mentioned before Rosendahl *et al.* [3] examined open channel flows between parallel plates. There two opposite aligned free surfaces constrict the cross-sectional area A^* and the local mean velocity at the smallest cross-section is higher than in a similar groove channel with only one free surface. For convective dominated flows the critical flow rate is therefore significantly lower. In contrary for friction dominated flows the local pressure is not dominated by inertia effects and friction losses are greater in groove channels. Therefore the critical flow rate for a parallel plate channel is higher than for a similar groove channel.

5 Summary

In this work we investigated experimentally and numerically forced liquid flows through open capillary grooves under microgravity conditions. The experimental investigations focused on the profile lines of the free surface contour and the maximum flow rate through the channel without a collapse of the free surface which is defined as the critical flow rate.

An one-dimensional flow model is presented in which the liquid pressure is related to the capillary pressure at the free surface including both principal radii of curvature. The flow model considers also the convective and viscous pressure losses. In the comparison of experimental and numerical data we focused our investigations on convective dominated capillary channel flows. For this regime we obtain a good agreement of our experimental and numerical data. So we are able to simulate these types of flow with our theoretical model numerically.

Furthermore we presented a derivation of the mechanism of flow rate limitation for these flow conditions which is similar to the Mach-Number problem for compressible gas flows. If the average flow velocity through the channel reaches the capillary wave speed the flow is choked and it is not possible to increase the volume flow through the channel. If this occurs, the free surface of the liquid collapses and gas is ingested into the channel.

Acknowledgements The funding of the research project by the German Federal Ministry of Education and Research (BMBF) through the German Aerospace Center (DLR) under grant number 50 WM 0241 and 50 WM 0535 is gratefully acknowledged.

Furthermore we acknowledge the fundamental help of Mr. H. Faust and Mr. R. Mairose for mechanical and electronic support.

References

1. D. E. Jaekle, J.: Propellant management device conceptual design and analysis: Vanes. In: AIAA/SAE/ASME/ASEE 27th Joint Propulsion Conference, AIAA 91-2172, pp. 1–13. AIAA, Sacramento, CA (1991)
2. D. E. Jaekle, J.: Propellant management device conceptual design and analysis: Sponges. In: AIAA/SAE/ASME/ASEE 29th Joint Propulsion Conference and Exhibit, AIAA-93-1970, pp. 1–13. AIAA, Monterey, California (1993)
3. Rosendahl, U., Ohlhoff, A., Dreyer, M.E.: Choked flows in open capillary channels: theory, experiment and computations. *J. Fluid Mech.* **518**, 187–214 (2004)
4. Gersten, K.: Einführung in die Stroemungsmechanik. Vieweg Verlag, Braunschweig (1991)
5. Dreyer, M.: Free Surface Flows under Compensated Gravity Conditions, *Springer Tracts in Modern Physics*, vol. 221. Springer-Verlag (2007)
6. White, F.M.: Fluid Mechanics. McGraw Hill, New York (1986)
7. Haake, D., Rosendahl, U., Ohlhoff, A., Dreyer, M.E.: Flow rate limitation in open capillary channel flows. *Ann. NY Acad. Sci.* **1077**, 443–458 (2006)
8. Landau, L.D., Lifschitz, E.M.: Lehrbuch der Theoretischen Physik, Band VI, Hydrodynamik. Akademie Verlag, Berlin (1991)
9. Bronstein, I.N., Semendjajew, K.A.: Taschenbuch der Mathematik. Teubner (1985)
10. Klatte, J., Haake, D., Weislogel, M.M., Dreyer, M.: A fast numerical procedure for steady capillary flow in open channels. *Acta Mech.* **201**, 269–276 (2008)
11. Grah, A., Haake, D., Rosendahl, U., Klatte, J., Dreyer, M.E.: Stability limits of unsteady open capillary channel flow. *J. Fluid Mech.* **600**, 271–289 (2008)
12. Baessmann, H., Besslich, P.W.: Bildverarbeitung ad oculos. Springer Verlag, Berlin (1991)
13. 3M: Fluorinert Electronic Liquid FC-72 (2000)